RSC Advances

PAPER

View Article Online
View Journal | View Issue

Cite this: *RSC Adv.*, 2024, **14**, 14100

Bicomponent core/sheath melt-blown fibers for air filtration with ultra-low resistance

Xiaofang Lin,[ab] Wenbo Sun,[a] Minggang Lin,[a] Ting Chen,[b] Kangming Duan,[a] Huiting Lin,[ac] Chuyang Zhang[a] and Huan Qi *[ac]

With the escalating air pollution and frequent outbreaks of airborne diseases, there is a growing demand for personal protective filtration media. Melt-blown nonwovens have proven to be highly effective in capturing tiny particles, but their tightly packed fiber assemblages are more resistant to airflow and less comfortable to breathe. Here, we present a one-step melt-blown spinning process for the production of bicomponent core/sheath (BCS) crimped fibers and their application in high-efficiency, low-resistance air filtration. Fiber curl is caused by unbalanced internal stresses resulting from differences in the structure components, resulting in uneven shrinkage inside and outside the fibers. The resulting CM@S-2 filtration media features a uniform fiber curl and a porous fiber mesh structure, which reduces air filtration resistance. Under the same filtration conditions, the filtration efficiency of CM@S-2 (96.58% *vs.* 95.58%), filtration resistance (56.1 Pa *vs.* 108.0 Pa), quality factor (0.061 Pa^{-1} *vs.* 0.029 Pa^{-1}), and dust holding capacity (10.60 g m^{-2} *vs.* 9.10 g m^{-2}) were comparable to those of the single-component polypropylene filters. The filtration efficiency of the CM@S-2 remained above 94.0% after 30 days of indoor storage. Computational Fluid Dynamics (CFD) simulation demonstrated that crimped fibers effectively reduce pressure surges on the filter media caused by fiber accumulation. In comparative tests with commercial masks, the CM@S-2 cartridge masks demonstrated superior air permeability compared to commercial masks under similar filtration conditions. In conclusion, the bicomponent core/sheath melt-blown fibers significantly reduce air resistance and show excellent potential for application in protective masks.

Received 22nd March 2024
Accepted 21st April 2024

DOI: 10.1039/d4ra02174f

rsc.li/rsc-advances

1. Introduction

The issue of atmospheric pollution caused by particulate matter (PM) has garnered global attention, leading to the widespread use of masks as personal protective equipment (PPE).[1] PM refers to non-degradable particles and droplets suspended in the atmosphere, which consist of both inorganic and organic components. These particles are hazardous because they can transport significant amounts of toxic substances into the human body through respiration.[2–4] When the human body is chronically exposed to high concentrations of PM, its tiny size (aerodynamic equivalent diameter less than 0.3 μm) can transport pathogenic bacteria into the bloodstream, leading to significantly increased morbidity and mortality.[5,6] Masks are effective personal protective equipment for preventing individuals from inhaling harmful particles. Masks are typically made of nonwoven materials. Spunbonded and needle-punched fibers, typically with diameters in the tens of microns, are only suitable for coarse filtration and are commonly used as coverings or linings for masks. The most critical components of the masks consist of micro/nanofiber nonwovens with fiber diameters ranging from a few hundred nanometers to a few microns. Utilizing the structural characteristics of micro/nanofiber nonwovens, such as small fiber diameter, large specific surface area, excellent internal connectivity, and high porosity, fiber filters can be highly effective in capturing fine particulate matter in the air.[7–10]

Electrostatic spinning is acknowledged as an effective technique for producing nanofibrous membranes with a high specific surface area, well-connected internal structure, and controllable morphology. These characteristics play a crucial role in significantly enhancing filtration efficiency for the air filter.[11–13] Many researchers have developed fiber structures using electrostatically spun nanofibers, such as ribbons,[14] pleats,[15] mesh,[16] and convolutions[17] for air filtration to achieve low air resistance and high filtration efficiency. Unfortunately, most polymers require organic solvents for dissolution during the preparation process. The use of organic solvents leads to secondary pollution to the environment, and the residual organic solvents in the nanofiber membranes pose hazards to human health,[18–20] thereby restricting the industrial production of electrostatic spinning technology.

[a]*Institute of Smart & Ecological Textile, Quanzhou Normal University, Fujian, China. E-mail: qhqh123@126.com*
[b]*College of Textile and Clothing Engineering, Soochow University, Jiangsu, China*
[c]*College of Textile and Apparel, Quanzhou Normal University, Fujian, China*

Currently, the filter media of commercial masks is typically manufactured using melt-blown spinning technology. Melt-blown fibers are produced by extruding hot melt polymers at specific temperatures through a screw extruder, supplemented by hot air blowing and fiber-spreading to obtain micron-sized fiber filters. The diameter of the melt-blown fiber (1.0–3.0 μm) is larger than that of the electrostatically spun fibers (50–500 nm), resulting in lower filtration performance compared to electrostatically spun filter media.[21,22] Therefore, the melt-blown filter needs to undergo an electrostatic electret treatment to enhance its filtration performance. Filtration efficiency and filtration resistance are crucial factors for assessing the filtration performance of filter media. It is essential to develop filtration materials that can provide effective protection while also allowing for comfortable breathing. Significant research has been conducted to improve the quality factor (high filtration efficiency and low resistance) of melt-blown filters by optimizing the spinning conditions, reducing the fiber fineness, designing the mesh structure, and optimizing the electret.[23–25] Ma *et al.* achieved a high filtration efficiency in a composite filter by alternating the arrangement of ultra-thin nanolayers and melt-blown layers, which built up layer-by-layer interception and collaborative filtering effects.[23] Zhu *et al.* added silica (SiO_2) nanoparticles to poly (lactic acid) (PLA) melt-blown fabrics to improve the charge storage stability and to realize the high efficiency and low resistance filtration performance of melt-blown nonwoven fabrics.[25]

Crimped fibers are also used for air filtration to enhance the filter fluffiness. Zheng *et al.* fabricated curled PVDF nanofiber membranes through electrospinning, which demonstrated lower filtration resistance and higher dust holding capacity compared to uncurled fibers.[26] In addition to electrostatic spinning, curly fibers have also been reported in melt spinning. Fiber crimping can be achieved by capitalizing on the variations in contraction of different polymers during the melting spinning process. Hui *et al.* selected polyurethane (TPU) and polypropylene (PP) to produce a curly fiber nonwoven using a specially designed rotary-flow mold melt-blown device.[27] Due to the poor compatibility between PP and TPU, the fibers with a curly structure cannot be formed stably during spinning. Lin *et al.* used a blend of polypropylene with varying properties to manufacture a micron-sized crimped melt-blown filter.[28] The crimped fibers create a fluffy filter structure, which effectively reduces filtration resistance while maintaining high filtration efficiency. However, these filters have been produced by melt-blown spinning with direct blending. The uniformity of the fibre curl may be affected by differences in the compatibility of the raw materials and the uniformity of the blend.

To address a series of issues stemming from the incompatibility between polymers in mixed spinning, researchers have investigated two-component spinning techniques, such as core–sheath, side-by-side and matrix.[29,30] Among them, the core–sheath fiber has been widely used. For instance, nanofibers with a core–sheath structure are produced by electrospinning, which gives the fibers a stable structure and excellent mechanical properties, making them suitable for applications in the fields of medical and health materials.[31,32] To the author's knowledge, there are fewer reports on the use of core–sheath melt-blown fibers for air filtration. Therefore, the design of core–sheath melt-blown fibers to achieve high filtration efficiency and low resistance is crucial for the advancement of high-performance nonwovens.

In this study, a melt-blown nonwoven filter was created using two-component core–sheath crimped fibers to achieve high filtration efficiency and low air resistance. The differential shrinkage of the fiber cortex and core layers facilitated uniform fiber crimping and ensured the permeability of the filter. We focused on fiber diameter, pore size, porosity, surface potential, and filtration properties, including various particulate matter (PM) filtration characteristics, recirculation filtration, and 30 day filtration efficiency. To investigate the performance of air passing through a melt-blown fabric with crimped fibers, airflow field simulations were conducted to analyze the pressure distribution within the melt-blown fabric during the filtration process. Finally, a mask was successfully fabricated using the designed nonwoven cartridge, and the breathability of the mask was evaluated. This straightforward method will produce a low-pressure drop cartridge for the mask, providing more comfortable personal medical protection.

2. Materials and methods

2.1. Materials

Polypropylene (PP) pellets (Y1500, 0.7386 g cm^{-3} density) with a melt flow rate (MFR) of 1800 g/10 min at 230 °C were purchased from China-Base Petrochemical Co., Ltd. Crimped masterbatch (CNF01, 0.8288 g cm^{-3} density, MFR = 700 ± 100 g/10 min at 210 °C), referred to as CM, were supplied by Keimei Plastifizierung Technik (Yantai) Co., Ltd.

2.2. Fabrication of melt-blown nonwovens

PP/CM core–sheath fibers were prepared using SMS300-Bico-M bicomponent melt-blown equipment (SMS300-Bico-M, KMD Plastifizierung Technik GmbH, Lübeck, Germany), where component A corresponds to the sheath of the fiber and component B corresponds to the core of the fiber. Firstly, the PP and PP/CM mixture (8 : 2 or 7 : 3, w : w) were dried and put into hopper A or B respectively. Secondly, the polymers form two different polymer melts in their separate feedstock output systems and distribution channels. Eventually, the molten polymer converged at the die head and flowed out of the spinneret, where it was extruded by hot air to create core–sheath fibers. Unless otherwise noted, the base weight of the melt-

Table 1 Melt-blown nonwovens

Component A (sheath)	Component B (core)	Samples
Pure PP	Pure PP	PP
Pure PP	PP/CM (8 : 2)	CM@C-1
PP/CM (8 : 2)	Pure PP	CM@S-1
Pure PP	PP/CM (7 : 3)	CM@C-2
PP/CM (7 : 3)	Pure PP	CM@S-2

Table 2 Processing conditions of melt-blown nonwovens

Screw zone 1–5/°C	Die/°C	Air/°C	Pump flow/cc min^{-1}	Air fan/Hz	DCD[a]/mm
180/200/220/240/260	260	270	50	PP:19 CM@C:21 CM@S:22	300

[a] DCD is the distance from the spinning die to the fiber collector.

blown materials was about 30 g m^{-2}. Table 1 shows the core–sheath fibers with different PP/CM ratios. The processing conditions of melt-blown nonwovens are listed in Table 2.

2.3. Corona charging

The melt-blown nonwovens were subjected to electret treatment using a double-sided corona charging device (CWZJT-3, Nantong Sanxin Plastic Equipment Technology Co., Ltd, Nantong, China). The device comprises a high-voltage power supply and two sets of electrode wires. The sample was positioned between the electrode wire and the substrate. After applying a high voltage, charges are deposited on both sides of the melt-blown material, resulting in a double-sided electret effect. The applied voltage was 60 kV, and the charging time ranged from 10 to 30 seconds.

2.4. Characterization

The surface elements of feedstocks were analyzed by energy-dispersive X-ray spectrometer (EDS, Thermo Scientific Helios 5 CX, Thermo Fisher Scientific, Waltham, MA, USA). The Fourier transform infrared (FTIR) spectra of crimped masterbatch and melt-blown nonwovens were analyzed using a Fourier transform infrared spectrometer (Thermo Fisher Nicolet iS5, Thermo Fisher Scientific, Waltham, MA, USA). The thermal stability information of the melt-blown nonwovens was obtained through a thermogravimetric analyzer (TA-Q500, TA Instruments, USA). The surface morphology of melt-blown fiber was investigated by scanning electron microscope (SEM) (TESCAN MIRA LMS, Tescan China Ltd, Shanghai, China) after sputter-coating the samples with gold. The diameter and distribution of 200 random fibers were analyzed using Nano Measurer 1.2 software. The melt-blown fabrics were subjected to orientation analysis using the DHU-11 nonwoven fiber network orientation analysis system. The pore diameter of the melt-blown nonwovens was measured using a capillary pore diameter analyzer (CFP-1500-AEXL, Porous Materials Inc., Ithaca, NY, USA). The surface potential of PP/CM nonwovens was tested on a non-contact electrostatic field meter (FMX-004, Simco Japan Inc., Kobe, Japan).

The filter thickness was measured using a digital display thickness gauge (EVERTE CHYQFP25.4, Bon Agent Measuring Tools Co., Ltd, Shangqiu, China), and the average thickness was determined by taking measurements at 20 different points on the sample. The porosity P of the filter is calculated according to eqn (1) and (2).

$$P = \left[1 - \frac{s}{\rho \times t}\right] \times 100\% \quad (1)$$

$$\rho = \rho_{pp} \times W_{pp} + \rho_{CM} \times W_{CM} \quad (2)$$

where s is the surface density of the sample, t is the sample thickness, ρ is the density of the sample, ρ_{pp} is the density of PP, W_{pp} is the proportion of PP mass, ρ_{CM} is the density of CM, W_{CM} is the proportion of CM mass.

The mechanical properties of different masks were tested using an electronic fabric strength machine (YG026HB, Quanzhou Meibang Instrument Co., Ltd, Quanzhou, China). The samples were 50 × 150 mm, the drawing rate was 100 mm min^{-1}, and the drawing distance was 100 mm.

The air permeability of the masks was measured using a digital fabric permeability meter (YG461E, Quanzhou Meibang Instrument Co., Ltd, China) according to the GB/T5453-1997 standard. Meanwhile, we developed and built a device to measure water vapor permeation through the CM@S-2 mask, which directly demonstrated its exceptional air permeability.

2.5. Filtration performances

The filtration performance and pressure drop of melt-blown nonwovens were measured using a particle filtration efficiency tester (DR251XL, Wenzhou Darong Textile Instrument Co., Ltd, Wenzhou, China) in accordance with GB 2626-2019. The concentration of the sodium chloride (NaCl) aerosol solution was 2.0 wt%, and the particle diameter followed a normal distribution with a median diameter of 0.075 μm and a geometric standard deviation of less than 1.86. Aerosol particles were passed through the 100 cm^2 testing area at a flow rate of 85 L min^{-1}. The filtration efficiency was determined by measuring the concentration of aerosol particles both upstream and downstream of melt-blown nonwovens. The filtration efficiency of PM0.3 particles was recorded and evaluated. The filtration efficiency (η) is calculated using the following equation:

$$\eta = \frac{C_{up} - C_{down}}{C_{up}} \times 100\% \quad (3)$$

where C_{up} and C_{down} represent the concentration of aerosol particles in the upstream and downstream of melt-blown nonwovens, respectively.

The pressure drop is calculated by measuring the gas pressure difference between the upstream air inflow side and the downstream air outflow side of the filter material. The pressure drop (ΔP) is calculated by the following formula:

$$\Delta P = P_1 - P_2 \quad (4)$$

where P_1 is the pressure before filtration and P_2 is the pressure after filtration.

Since filtration efficiency and pressure drop are conflicting, neither of them is valid for assessing the filtration performance of melt-blown nonwovens alone, so the quality factor is used to comprehensively assess the filtration performance of the material. The larger the quality factor, the better the filtration performance of the material. The quality factor (QF) is calculated by the following formula:

$$\mathrm{QF} = -\frac{\ln(1-\eta)}{\Delta P} \quad (5)$$

The dust holding capacity and pressure drop growth rate are important indicators to characterize the service life of the filter material. A filtration loading test was performed to investigate the dynamic filtration property according to GB 2626-2019 and NIOSH Standards (Title 42 CFR Part 84) for N95. The dust holding capacity of melt-blown nonwovens was also evaluated by DR251XL, which is defined as the mass of particles deposited on the filter per unit area when the initial pressure drop doubles. The NaCl aerosol solution concentration was adjusted to 5.0 wt% and the air flow rate remained at 85 L min^{-1}. The dust holding capacity is calculated by the following equation:

$$D = \frac{(m_1 - m_0)}{A} \quad (6)$$

where m_1 is the mass of the filter material after dust tolerance, m_0 is the mass of the filter material, and A is the effective filter area of the filter material.

A realistic smoke environment was simulated by burning cigarettes to evaluate the filter's effectiveness in capturing particulate matter (PM). The dust particle counter (AIRHUG-CP-15, Beijing Yishan Technology Co., Ltd) was utilized to measure the PM concentration before and after burning cigarettes.

2.6. Airflow field simulation

To simulate the airflow field around the samples, a three-dimensional (3D) model was generated using SOLIDWORKS software, incorporating the parameters of the prepared samples. The 3D structural models were imported, and the Fluent module of ANSYS 2023R1 software was used to conduct the simulations. The inlet airflow velocity was set to 0.1 m s^{-1}, and the outlet pressure was set to 0 Pa for the filtration experiments.

3. Results and discussions

3.1. Structure of core/sheath melt-blow fiber

The physical structure of the fibers has a significant impact on the filtration performance and resistance of melt-blown filter materials.[33,34] By modifying the physical structure of melt-blown fibers and applying corona charging treatment, it is possible to improve the physical interception and electrostatic adsorption effects of melt-blown materials, while simultaneously reducing filtration resistance. This enables the production of high-efficiency, low-resistance melt-blown materials for air filtration. Firstly, the morphology and internal structure of melt-blown fibers determine their physical capacity to trap particles.[35] The intricately structured design of filters can extend the contact time between the fibers and particles in the thickness direction, thereby increasing the likelihood of the melt-blown fibers capturing PM. Secondly, corona electret treatment of the melt-blown nonwovens increases the charge density on the fiber surface, improving its ability to trap particles. This further enhances filtration efficiency through electrostatic adsorption.[36–38] In addition, the air filter material must have high porosity to ensure efficient air flow. The crimped structure of the fiber can increase the pore size and porosity of melt-blown nonwovens, leading to a fluffy composite and reduced filtration resistance.

PP or PP/CM blend is used as the core or sheath of the fiber, respectively. The fiber structure is altered by inducing uneven contraction between the polymers through temperature changes. This process creates a three-dimensional curled structure, which enhances the fluffiness and porosity of nonwoven filter. However, fiber structures with excessive porosity and fluffiness can cause particles to pass more smoothly through the airflow, leading to suboptimal filtration performance. By adjusting the ratio and distribution of PP and CM, the positive or negative effects of the fiber curl structure on the filtration performance are combined, ensuring that the filtration performance of the fiber mesh is maintained at a high level. Based on the aforementioned ideas and strategies, as illustrated in Fig. 1(a), we employed one-step melt-blowing technology to fabricate bicomponent core/sheath self-crimped fiber filter materials. Fig. 1(b) illustrates the corona charging process, and the CM also incorporates nanocomposite electret technology, so that the PP/CM melt-blown nonwoven material to provide a substantial amount of space for storing charge, facilitating the electrostatic adsorption of particles. The synergistic effect of physical interception and electrostatic adsorption in crimped fiber melt-blown fabrics results in excellent filtration performance, making them a promising option for air filtration (Fig. 1(c)).

To investigate the impact of the bicomponent core/sheath structure on the crimping properties of the fibers, PP/CM blends while the core or sheath of the fibers was PP. The structural morphology was observed using SEM, and the results are shown in Fig. 2(a)–(e). During the melt-blown process, it is observed that the polypropylene (PP) fibers do not experience uneven shrinkage due to temperature changes. Instead, the fibers maintain a columnar form. When the fiber sheath or core is blended by CM, unequal internal stresses develop within the fibers. As these internal stresses are relaxed, the fibers shrink and take on a woolly crimped form. Fiber curl increases progressively as the proportion of CM increases, leading to intensified uneven internal stresses within the fibers. In addition, when PP/CM is used as the fiber sheath, it exhibits a higher degree of curling compared to when used as a core. During the melt-blown process, the curling in the core layer of PP/CM caused by temperature changes may be mitigated by the PP in the sheath layer, leading to an undesirable curling effect.

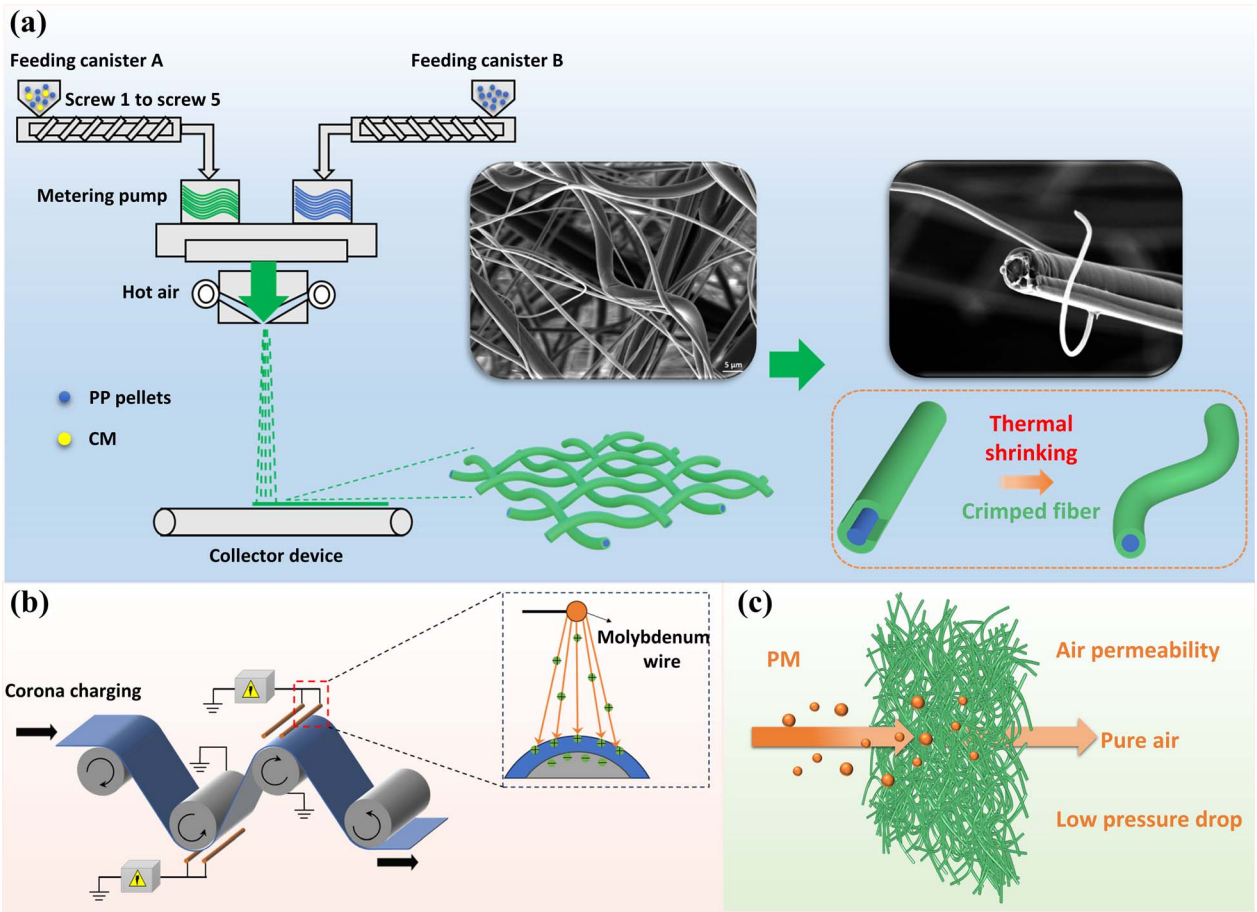

Fig. 1 (a) Fabrication of bicomponent core/sheath fibers. (b) Corona charging process. (c) Application of convoluted fiber melt-blown nonwoven in air filtration.

The diameter of the melt-blown fibers plays a crucial role in filtration performance.[39] To develop high-efficiency and low-resistance filter materials capable of effectively filtering micron-sized particles from the air through physical interception, we conducted additional research on the influence of the CM ratio and core/sheath distribution on fiber diameter. By controlling the composition of the CM and its dispersion in fibers, BCS melt-blown fibers with varying diameters were prepared as depicted in Fig. 2(f)–(j). The fibers exhibit an irregular stacked structure, and their diameters are less than 10 μm, following a normal distribution. The average fiber diameters of PP, CM@C-1, CM@S-1, CM@C-2, and CM@S-2 are 2.24 μm, 2.39 μm, 2.31 μm, 2.42 μm and 2.46 μm, respectively. The melt flow rate of polypropylene (PP) is 1800 g/10 min, which is significantly higher than that of CM. As the CM content increases, the entanglement between PP and CM polymer chains also increases, resulting in a higher viscosity of the PP/CM melt. This makes it more difficult for the melting polymers to be stretched by hot air, leading to a gradual increase in the average fiber diameter. The diameter data indicate that when the PP/CM blends are used as either the sheath or core layer of the fibers, the fiber diameters of both are similar. For example, CM@C-1 and CM@S-1, as well as CM@C-2 and CM@S-2, exhibit similar diameters, indicating that the core/sheath structure does not significantly affect the fiber diameters of the same polymers.

3.2. Chemical element and thermal stability analysis

The content and distribution of C, O and N elements in PP and CM were explored by an energy spectrum instrument, as shown in Fig. 3(a) and (b). EDX spectra showed that the carbon element was uniformly distributed on the entire surface of PP and CM, and the content was similar between these two species. This was consistent with the information provided by the supplier that CM was a class of curly masterbatch blended with PP and PE. To further validate this result, the chemical structure of PP and CM was investigated by FTIR in Fig. 3(c). From the results, the signal peaks at 2948 cm^{-1} and 2865 cm^{-1} were the stretching vibration carbon–hydrogen bond in $-CH_3$. The signals at 2916 cm^{-1} and 2836 cm^{-1} were the stretching vibrations carbon–hydrogen bond in $-CH_2-$. The bending vibration signals of $-CH_2-$ and $-CH_3$ were 1457 cm^{-1} and 1375 cm^{-1}, respectively. The infrared spectra of PP and CM were less different, indicating that the main component in CM was still polypropylene. However, there was an oscillating vibration peak at 747 cm^{-1} from continuous methylene, which was not appeared in PP, indicating the presence of polyethylene in CM.

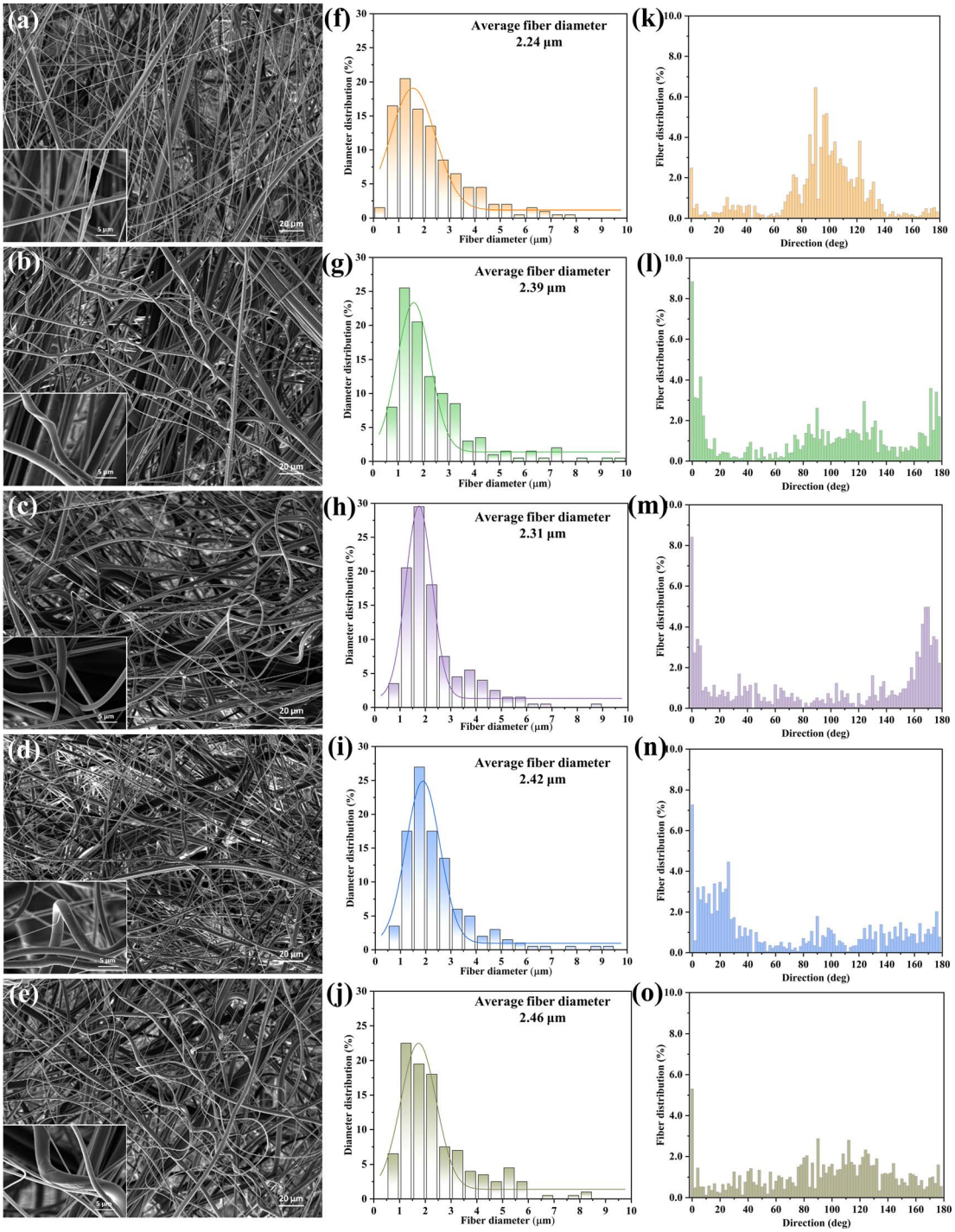

Fig. 2 SEM images of melt-blown webs of (a) PP, (b) CM@C-1, (c) CM@S-1, (d) CM@C-2 and (e) CM@S-2. Fiber diameter distribution of melt-blown webs of (f) PP, (g) CM@C-1, (h) CM@S-1, (i) CM@C-2 and (j) CM@S-2. Fiber orientation distribution of melt-blown webs[31,32] of (k) PP, (l) CM@C-1, (m) CM@S-1, (n) CM@C-2 and (o) CM@S-2.

Thermogravimetric analysis was conducted on CM plastics and PP/CM melt-blown fibers to evaluate their thermal stability. The results are presented in Fig. 3(d). The derivative thermogravimetry (DTG) curves indicated that CM, PP, CM@S-1 and CM@S-2 exhibited the highest rates of decomposition at approximately 475 °C. At this temperature, the weight loss rates were 65.37%, 59.78%, 56.42% and 60.87% respectively. This stage is the main weightless phase of the polymer, where the macromolecular chains are highly decomposed. As the amount of CM increased, the decomposition temperature of PP changed less. This suggests that CM and PP have the similar thermodynamic properties. The addition of CM has a minimal effect on the thermal performance of PP. The thermal degradation process of the PP/CM blends was found to be similar at different levels of CM content.

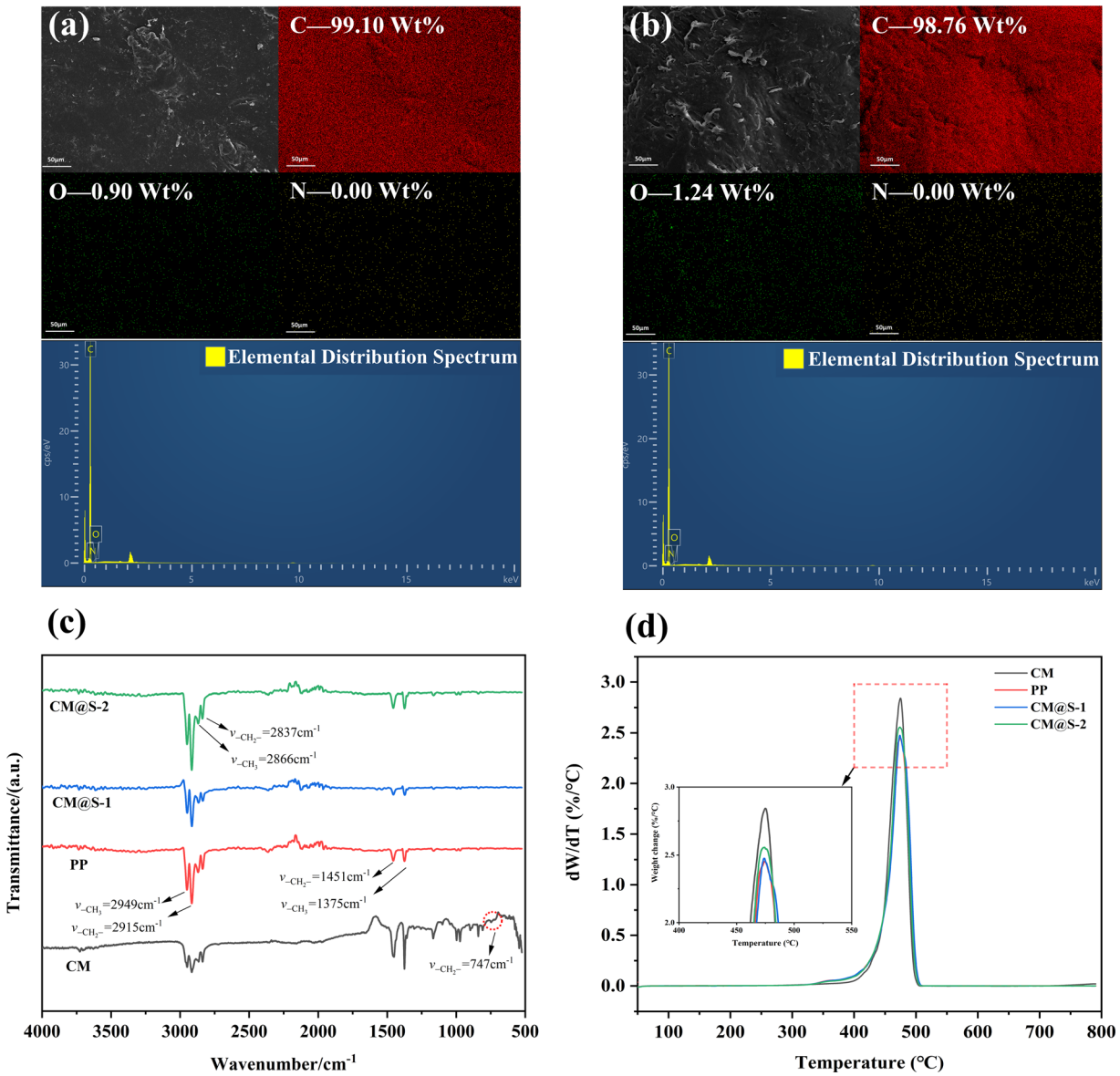

Fig. 3 EDX images of (a) PP and (b) CM plastic. CM, PP, CM@S-1, CM@S-2 (c) FT-IR and (d) DTG.

3.3. Fiber-web structure and surface potential

The fiber-web orientation analysis system (DHU-11, Donghua University, China) was utilized to analyze the orientation of BCS fibers in the filter. Image processing technology is used to extract the double edge whorl of the fibers in the SEM image. The fiber segment orientation angle is calculated using the boundary line integration algorithm and then statistically grouped to achieve the fiber orientation distribution of the material across the full angular range of 0–180°. As shown in Fig. 2(k)–(o), the fiber orientation of PP, CM@C-1, and CM@S-1 is concentrated with a high degree of alignment. The bending of CM@C-2 and CM@S-2 fibers increased the intricacy of the local fiber orientation within the fiber network, leading to a broader distribution of fiber orientation and a reduced degree of orientation.

A thickness gauge was used to investigate the impact of crimp morphology on the composite fluffiness, and the results are presented in Fig. 4(a) and (b). The PP, CM@C-1, CM@S-1, CM@C-2 and CM@S-2 present similar surface densities, while the thicknesses slightly increase within the range of 0.245–0.362 mm with higher CM content. Among these, the PP melt-blown filter has a minimum thickness of 0.245 mm. This is because pure polypropylene (PP) has a higher melt index and fluidity than PP/CM, making it easier to produce fine fibers that are relatively densely packed. Furthermore, the inclusion of CM into PP causes the fiber to curl and increases the degree of fluffiness.

Melt-blown filters with multi-scale pore sizes and high porosity are crucial for achieving high efficiency and low resistance. Fig. 4(c) illustrates the pore size distribution of the BCS melt-blown nonwovens. The pore sizes exhibited a bimodal distribution, with concentrations around 10.0 μm and 23.0 μm, respectively. This may be attributed to the influence of the flow

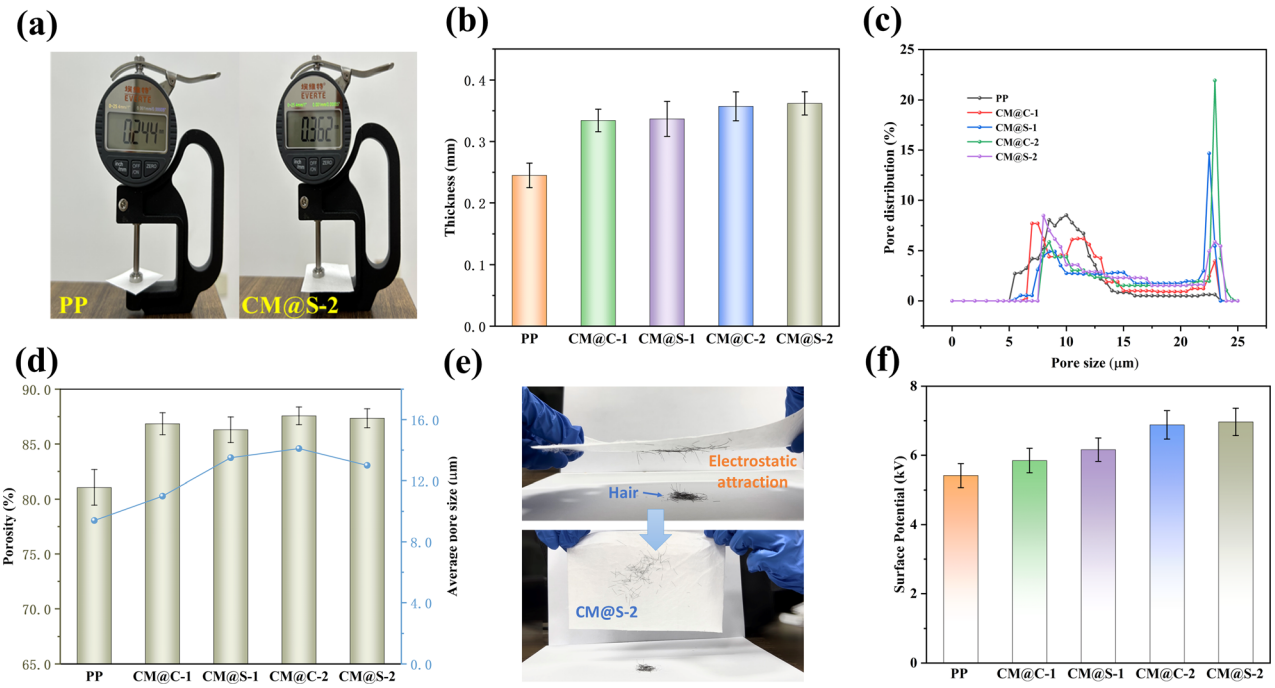

Fig. 4 (a) Digital photo of thickness measurement of PP and CM@S-2. (b) Thickness, (c) pore size distribution and (d) average pore size and porosity of melt-blown nonwovens. (e) Photograph showing the absorption of hair onto the CM@S-2 melt-blown nonwoven with high electrostatic attraction. (f) The surface potential of melt-blown nonwovens as a function of the CM content and distribution.

characteristics of the polymer melt and the spinning process parameters. The average pore sizes of PP, CM@C-1, CM@S-1, CM@C-2 and CM@S-2 were 9.4 μm, 11.0 μm, 13.5 μm, 14.1 μm and 13.0 μm, respectively. This is mainly due to the increase in the fluffiness of the fiber network. The fewer the number of fibers per unit volume, the larger the pores formed by the overlap between the fibers. The results showed that the crimping masterbatch was able to alter the pore size structure and distribution of PP melt-blown nonwovens. Furthermore, the pore size of the melt-blown filter showed significant improvement after being mixed with CM.

Porosity is the volume of pores as a percentage of the total volume. The size of the porosity directly reflects the degree of compactness of the filter. Fig. 4(d) shows the porosity of different melt-blown filters, and it is observed that the porosity of pure PP is only 81.1%, while the CM@C-2 and CM@S-2 have the higher porosity of 87.0%. The results confirmed that the composite porosity shows a slow growth trend with the CM ratio. High porosity nonwoven composite helps to reduce the surface pressure.[40,41]

The CM utilizes nano-composite electret technology. The charge stored in the electret enhances the electrostatic potential on the surface of the filter, thereby improving the filtration efficiency of sub-micron particles.[42] The PP/CM BCS melt-blown nonwoven material exhibits strong electrostatic attraction, which causes fragmented hair to be drawn to the CM@S-2 filter by electrostatic force (Fig. 4(e)). To demonstrate the improved charge storage capacity and stability of CM, the surface potentials of different melt-blown nonwovens at steady state are shown in Fig. 4(f). It is clear that CM improves the ability to trap charges. The surface potential of pure polypropylene (PP) is the lowest at 5.41 kV. When the content of CM reaches 30 wt%, the potential increases from 5.41 kV to 6.88 kV (CM@C-2) and 6.97 kV (CM@S-2). During the process of producing melt-blown electret composite, high voltage is applied to the surface through corona discharge, and the injected charge is distributed within a thin layer of 2.0–10.0 μm on the filter surface. Therefore, the surface potential of the sheath layer in PP/CM fiber is slightly higher than that of the core layer in PP/CM fiber.

3.4. Filtration performance

Meltblown nonwovens possess the characteristics of a large specific surface area, small pore size and high porosity. The three-dimensional disordered network packing structure makes it an excellent filtering material. However, when the high-speed air passes through the meltblown material, it is obstructed by the holes in the fiber mesh, leading to a reduction in air flow rate and creating resistance. To evaluate the influence of CM on the filtration efficiency and air resistance of polypropylene (PP) nonwovens, the samples were tested for filtration efficiency and pressure drop at high speed (85.0 L min^{-1}) and low speed (32.0 L min^{-1}) flow rates. Fig. 5(a) depicts the filtration performance of the melt-blown material against particles that penetrate (approximately 0.3 μm in size) at an airflow rate of 85.0 L min^{-1}. The filtration efficiency of PP, CM@C-1, CM@S-1, CM@C-2 and CM@S-2 was 95.58%, 95.98%, 97.22%, 94.94% and 96.58%, respectively. Additionally, CM@S-1 and CM@S-2 maintained a high level of filtration efficiency. The filtration mechanism is primarily divided into mechanical barriers and electrostatic

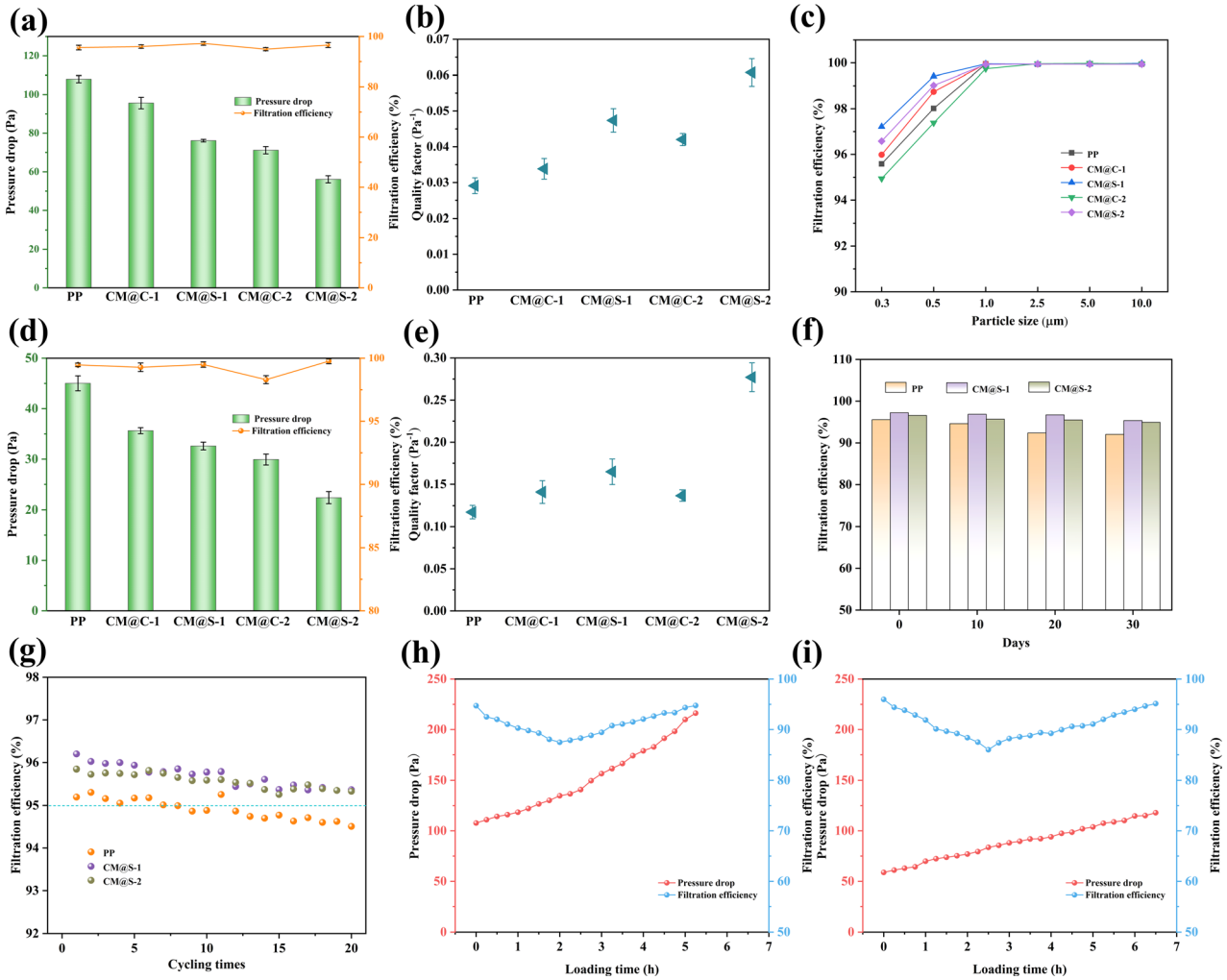

Fig. 5 (a) The filtration efficiency and pressure drop, and (b) the quality factor of melt-blown nonwovens for PM0.3 under 85 L min^{-1}. (c) Filtration efficiency *versus* particle size. (d) The filtration efficiency and pressure drop, and (e) the quality factor of melt-blown nonwovens for PM0.3 under 32 L min^{-1}. (f) Decay of filtration efficiency within 30 days. (g) Cycling filtration performance of melt-blown nonwovens for PM0.3 under 85 L min^{-1}. (h) Filtration efficiency and pressure drop of PP during loading. (i) Filtration efficiency and pressure drop of CM@S-2 during loading. The detection particle size is ~0.3 μm in subfigures (h) and (i).

adsorption.[43,44] The mechanical barrier depends on small fiber diameter and high specific surface area to increase the probability of collision and interception between fibers and particles. Electrostatic adsorption relies on coulombic forces to attract and trap charged particles directly in the gas phase. The convoluted structure of CM@S-1 and CM@S-2 acts as a mechanical barrier, increasing the thickness of the melt-blown nonwovens and extending the filtration time for particles in the material. However, the fiber diameters and pore sizes are significantly larger than those of PP, which makes it easier for airflow to carry particles through the melt-blown nonwovens. Electrostatic adsorption has an excellent filtration effect on particles with a size of less than 1.0 μm. CM@S-1 and CM@S-2 exhibit greater potential on the surface and can store more charge in the fibers. This enables them to more effectively filter submicron particles in the gas carrier phase and improve filtration efficiency. The results indicated that CM@S-1 and CM@S-2 improved filtration efficiency primarily through electrostatic adsorption.

The histogram in Fig. 5(a) illustrates that the proportion and distribution of CM significantly impact the pressure drop of melt-blown filters. The maximum pressure drop for PP is 108.0 Pa, while CM@S-2's is only 56.1 Pa, approximately 50% less than PP. The resistance level at the same air flow rate is influenced by the structural design of the filter, including pore size, porosity, thickness and fluffiness. The smaller diameter of PP fiber results in the formation of narrower gaps between the fibers, leading to a higher density of fiber deposition in the thickness direction and consequently greater filtration resistance. The haphazardly interwoven fibers of the CM@S-2 not only form countless barriers to particles, but the wide spaces between the crimped fibers also facilitate smooth airflow, resulting in minimal air resistance. Fig. 5(b) illustrates the quality factor (QF) of BCS melt-blown nonwovens for PM0.3

filtration. QF is the ratio of filtration efficiency to filtration pressure drop. CM@S-2 exhibits higher filtration efficiency and lower filtration pressure drop, leading to a higher quality factor compared to other BCS melt-blown nonwovens. Therefore, CM@S-2 has superior filtration performance.

To evaluate the appropriateness of BCS melt-blown filters for atmospheric conditions, filtration tests were conducted on salt particles of various sizes (Fig. 5(c)). The filtration efficiencies of all melt-blown samples significantly increased with the rise in PM levels. CM@S-1 exhibited higher filtration efficiencies for PM particle sizes less than 2.5 μm, with the filtration efficiencies of the samples reaching 99.90% when the PM particle size was larger than 2.5 μm. At a low flow rate of 32.0 L min^{-1}, the filtration efficiency of PP, CM@S-1 and CM@S-2 is all above 99.90% (Fig. 5(d)). The most notable difference in filtration pressure drop is between CM@S-2 and pure PP, with values of 22.40 and 45.02 Pa, respectively. At the same time, the QF of the CM@S-2 filter reaches 0.277 Pa^{-1} due to the reduced pressure drop and improved filtration efficiency under the influence of Coulomb force (Fig. 5(e)). Additional research was conducted to assess the stability of the filtration efficiencies of PP, CM@S-1 and CM@S-2 by testing the filtration efficiencies after exposing the samples to room conditions for 0, 10, 20 and 30 days. The results are presented in Fig. 5(f). The filtration efficiency decreases slightly due to a reduction in electrostatic adsorption caused by the neutralization of some of the charges in the fibers when exposed to moisture in the air. However, CM@S-1 and CM@S-2 still maintain a relatively stable filtration efficiency. After 20 cycles of filtration (Fig. 5(g)), the efficiencies of CM@S-1 and CM@S-2 remained above 95.00%, demonstrating favorable recycling performance for both materials. This further indicates that the PP melt-blown nonwoven with added crimped material exhibits excellent filtration performance and practicality.

Fig. 5(h) and (i) depict the filtration experiments conducted on salt particles using PP and CM@S-2, respectively. In the loading experiment, the filtration efficiency initially showed a tendency to decrease and then increase with the loading time, while the filtration resistance gradually increased. The loading test was halted when the resistance was doubled from its initial level. The dust capacity of PP was 9.10 g m^{-2}, while CM@S-2 had a capacity of 10.60 g m^{-2}. Furthermore, CM@S-2 took longer to reach twice the initial resistance, indicating that the fluffy-structured fiber assemblage had a longer lifespan.

3.5. Airflow field simulation

The airflow characteristics passing through the fiber components were further investigated, and the airflow field in the filtration process of PP and CM@S-2 nonwovens was numerically simulated using Fluent software. To simplify the calculations, the nonwoven porous region is modeled as a porous medium with an additional resistance source.[45] A three-dimensional model is developed using the structural parameters of nonwovens, such as thickness and porosity. This model encompasses both the fluid domain and the porous media domain.

The porous media model simulates the resistance of porous materials to fluid flow within the computational domain by incorporating a source term into the momentum equation. This source term consists of two components: the viscous resistance term and the inertial resistance term:[46]

$$S_i = -\left(\sum_{j=1}^{3} D_{ij}\mu v_j + \sum_{j=1}^{3} C_{ij}\frac{1}{2}\rho|v|v_j \right), \quad (i = x, y, z) \tag{7}$$

where S_i is the i-direction (x, y, z) momentum source term. D is the matrix of viscous drag coefficients. C is the matrix of inertial drag coefficients. μ is the viscous coefficient. ρ is the fluid density. $|v|$ is the value of the velocity, and v_j is the value of the velocity in the j-direction.

For the simple porous medium model, only the diagonal elements of the D and C matrices are retained, bringing $1/\alpha$ and C_2 into the diagonal terms of the D and C matrices in eqn (7). The simplified equation is as follows:

$$S_i = -\left(\frac{\mu}{\alpha}v_i + C_2\frac{1}{2}|v|v_i \right), \quad (i = x, y, z) \tag{8}$$

where α is the permeability, $1/\alpha$ is the coefficient of viscous resistance, and C_2 is the coefficient of inertial resistance.

The momentum source term acts on the fluid to produce a pressure gradient ΔP:

$$\Delta P = -S_i\Delta n = \left(\frac{\mu}{\alpha}v_i + C_2\frac{1}{2}|v|v_i \right)\Delta n, \quad (i = x, y, z) \tag{9}$$

where Δn is the thickness of the porous medium.[47]

The resistance coefficient is determined by experimental data that shows the relationship between the pressure drop (ΔP) and the velocity (v) of the porous medium. The calculated viscous resistance coefficients and inertial resistance coefficients were input into Fluent. The inlet and outlet conditions were set to a flow speed of 0.1 m s^{-1} and atmospheric pressure of 0 Pa, in accordance with the filtration experimental conditions. The simulation results for the pressure distribution of PP and CM@S-2 samples are depicted in Fig. 6(a) and (b). The simulation results indicate that the upper surfaces of PP and CM@S-2 experience the highest pressure, and the pressure decreases as the depth of the nonwoven material (the distance from the upper surface) increases. Since the outlet condition is atmospheric pressure and the pressure decreases from the highest value to zero along the direction of airflow, it is evident that the pressure of the PP melt-blown fabric is significantly higher than that of CM@S-2. The pressure difference between the upper and lower surfaces of the sample determines the pressure drop. The results indicated that the simulated pressure drops for PP and CM@S-2 nonwovens were 72.254 Pa and 37.573 Pa, respectively. The wool-like crimped fiber structure significantly reduced the pressure drop across the filters. This is because conventional PP meltblown fibers are rod-shaped, randomly oriented in the plane and densely stacked. Under high-velocity airflow, the fiber mesh surface physically intercepts particulate matter (PM), leading to a rapid increase in resistance. CM@S-2 melt-blown fibers are crimped to create a fluffy and porous 3D interpenetrating network structure that facilitates smoother airflow through the fiber aggregates,

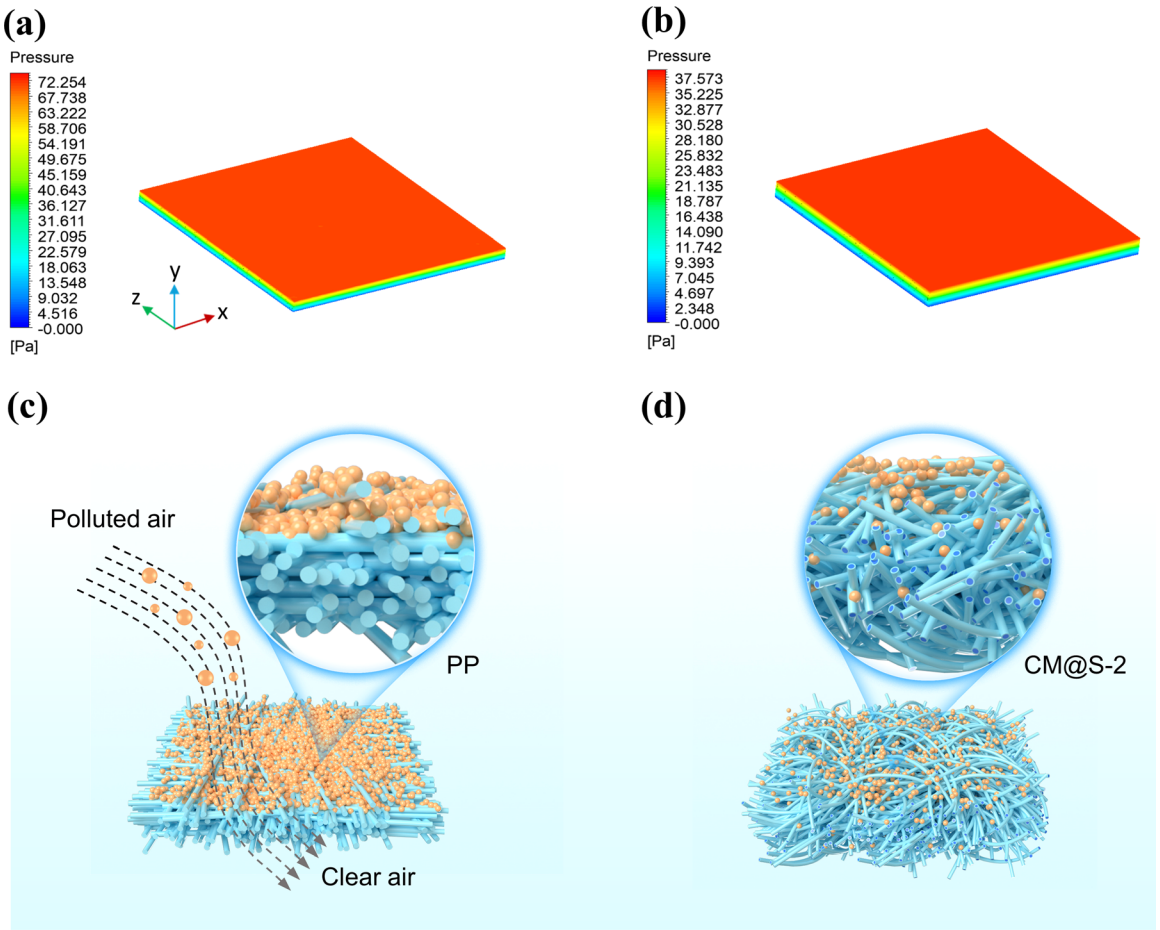

Fig. 6 Simulation of airflow field inside PP and CM@S-2 nonwovens. 3D diagrams of pressure distribution when the airflow passes through the inside of (a) PP and (b) CM@S-2 nonwovens. Cross-sectional views of particle loading on (c) PP and (d) CM@S-2 fibers (subfigures (c, d) were drawn using 3ds Max 2018 software).

resulting in reduced filtration resistance. As a result, CM@S-2 meltblown fibers with a crimped structure are expected to substitute conventional rod-shaped fibers, offering efficient and breathable air filtration.

3.6. Practical application of CM@S-2

Based on the analysis of filtration performance above, the crimped fiber of CM@S-2 was selected for further study. The melt blown filtration layer of a conventional surgical mask (surgical-mask 1) was replaced with CM@S-2 and reassembled into a protective mask with CM@S-2 as the core filtration layer (Fig. 7(a)).

The effectiveness of the CM@S-2 in cleaning smoke was determined by simulating an application in which the mask removes particles, as illustrated in Fig. 7(b). A cigarette was lit on the left side of the transparent box, and the PM2.5 counter showed heavily polluted air with an ultra-high concentration of PM2.5 ($\sim$6678 μg m^{-3}) in about 15 seconds. The CM@S-2 mask was placed in the center of two transparent boxes with continuous ventilation, and the PM2.5 levels remained at an excellent air quality for 3.0 minutes after lighting a cigarette. The CM@S-2 mask effectively intercepted and absorbed the PM, leaving the right side of the box clear and transparent, indicating that the prepared melt-blown fabric exhibits excellent filtration performance.[48]

To verify the practicality of the CM@S-2 mask for air filtration, the overall filtration performance in comparison to three commercial masks against PM0.3 and PM2.5 particles. As depicted in Fig. 7(c), at an airflow rate of 85.0 L min^{-1}, all masks achieved a filtration efficiency of 99.9% for PM2.5. The filtration efficiency of the CM@S-2 mask for PM0.3 was 96.85%, which was higher than that of medical mask 1 (94.10%), but lower than that of surgical mask 2 (99.54%) and KN95 (99.26%). In comparison, this mask has a lower filtration efficiency than surgical mask-2 and KN95, but it has a significantly lower pressure drop than other commercial masks. As depicted in Fig. 7(d), the pressure drops of the CM@S-2 mask is only 66.7 Pa, while the pressure drops of the surgical mask-2 and the KN95 are 139.8 Pa and 138.6 Pa, respectively, which are more than twice that of the CM@S-2 mask. Therefore, the CM@S-2 mask, which benefits from the twisted structure of the fibers, exhibits a higher quality factor compared to surgical masks and KN95, with quality factors of 0.052 Pa^{-1} and 0.113 Pa^{-1} for PM0.3 and PM2.5, respectively (Fig. 7(e)).

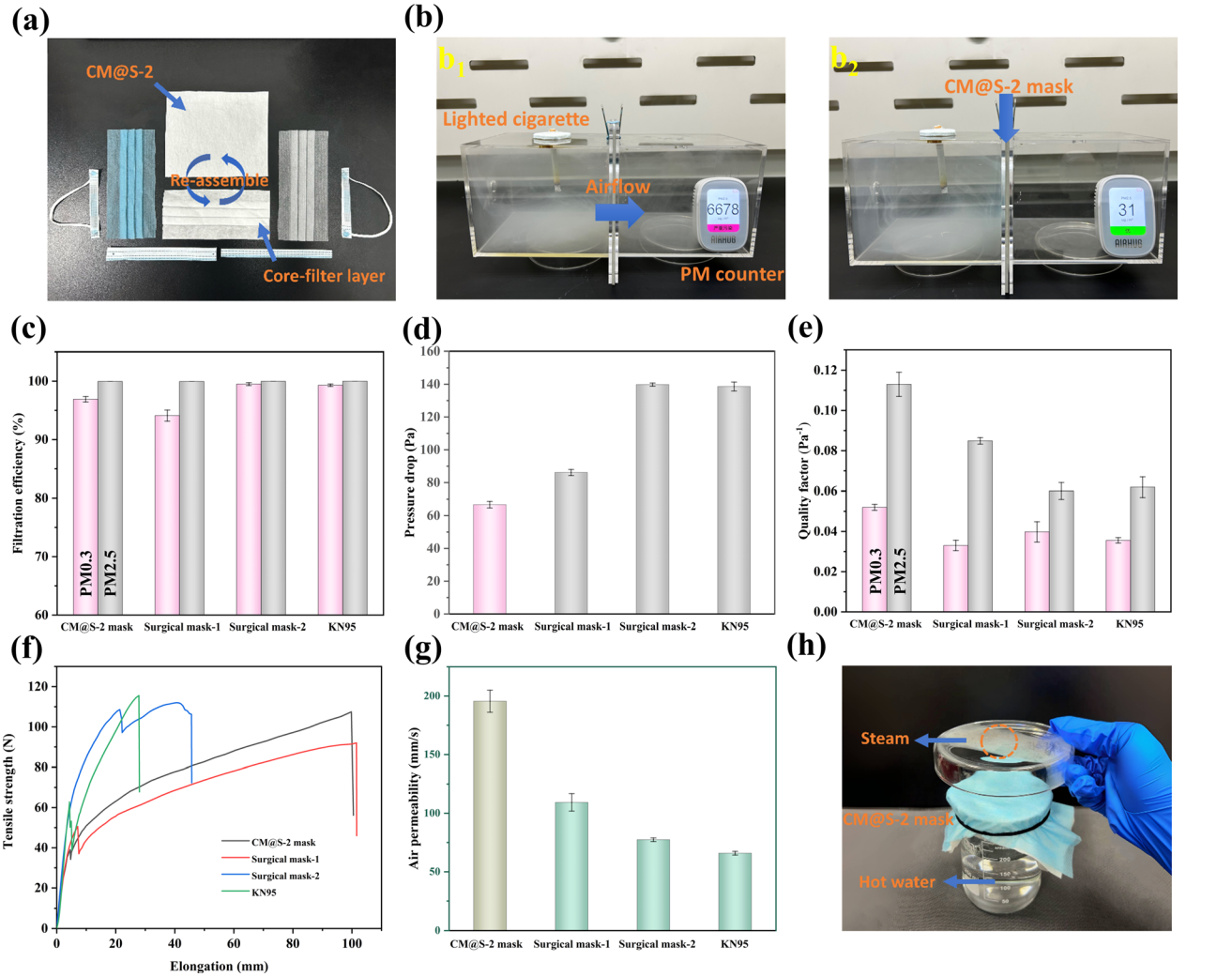

Fig. 7 (a) Crimped fiber re-assemble mask after replacing core-filter layer. (b) Filtration test system with the burning cigarette and a commercial particular counter. (b1) Number of PM2.5 without filter. (b2) Number of PM2.5 after filtration by CM@S-2 mask. (c) Filtration efficiency, (d) pressure drop and (e) quality factor of re-assembled CM@S-2 mask, common medical mask and KN95 mask for removing variously sized PM. (f) Tensile force and elongation of the commercial face masks and CM@S-2 mask. (g) Air permeability of the commercial face masks and CM@S-2 mask. (h) CM@S-2 mask digital photo of air permeability test.

Mechanical properties are the fundamental characteristics to evaluate melt-blown nonwovens. In practice, the mechanical properties of the mask are crucial to ensure effective filtration performance. The tensile strength *versus* elongation curves for different masks are depicted in Fig. 7(g). The tensile strength of the mask is mainly supported by the spun-bonded non-woven fabric in the outer layer. The tensile strength of our masks is comparable to that of surgical mask-1 and lower than that of surgical mask-2 and the KN95 mask. The CM@S-2 mask has a tensile strength of 107.5 N, ensuring its durability and comfort for wearers.

The air permeability of melt-blown nonwovens is another crucial factor for their suitability in air filtration applications. In everyday mask usage, the melt-blown layer plays a crucial role as the primary filtration layer, requiring exceptional filtration performance and breathability to meet the needs of human respiration. Fig. 7(g) illustrates the comparison of the air permeability performance of different masks. The CM@S-2 masks have the highest average air permeability at 195.56 mm s^{-1}, while KN95 masks have the lowest at 65.92 mm s^{-1}. The relationship between filtration resistance and breathability is inverse. A lower filtration resistance leads to improved breathability for the mask. We developed a device to measure the air permeability of this functional mask as shown in Fig. 7(h). The surgical mask (13 cm × 15 cm) was secured onto a beaker containing 200 mL of boiling water. The water vapor that passed through the mask condensed into droplets in the Petri dish positioned above the beaker, demonstrating the exceptional air permeability of the CM@S-2 crimped fiber nonwoven material.

4. Conclusion

In this study, meltblown filters with uniformly curled fibers were produced by controlling the preparation of sheath–core

components, which can be utilized for high-efficiency, low-resistance air filtration. By designing the sheath–core structure and optimizing its components, the CM curling component in the skin layer can achieve a more consistent curling effect of the fibers. The resulting CM@S-2 nonwoven filter media features a uniform fiber curl and a porous fiber mesh structure, which are crucial for achieving low air resistance. Aerodynamic simulations demonstrate that crimped fibers can effectively mitigate the pressure surge in the surface layer of the filter media caused by particle accumulation. This, in turn, reduces air filtration resistance and increases the dust holding capacity. Under the same filtration conditions, CM@S-2 demonstrates comparable filtration efficiency (96.58% *vs.* 95.58%), lower filtration resistance (56.1 Pa *vs.* 108.0 Pa), higher quality factor (0.061 Pa^{-1} *vs.* 0.029 Pa^{-1}), and superior dust holding capacity (10.60 g m^{-2} *vs.* 9.10 g m^{-2}) compared to a commercial single-component polypropylene filter. After 30 days of indoor storage, CM@S-2 maintained a filtration efficiency of over 94%. Masks made with CM@S-2 nonwovens as filter cartridges exhibited better breathability than commercial masks, suggesting that the pleated meltblown filter material provides a more comfortable wearing experience. The results suggest that this nonwoven material has the potential to be used in personal protective masks.

Conflicts of interest

There are no conflicts to declare.

Acknowledgements

This research was funded by the Fujian Provincial Co-innovation Platform Project Program (No. 2021FX08). The authors are grateful to the Apparel of QNU for providing laboratory facilities.

Notes and references

1 X. Zhang, J. Liu, H. Zhang, J. Hou, Y. Wang, C. Deng, C. Huang and X. Jin, *Polymers*, 2021, **13**, 485.
2 J. Colmer, I. Hardman, J. Shimshack and J. Voorheis, *Science*, 2020, **369**(6503), 575–578.
3 L. Liao, W. Xiao, M. Zhao, X. Yu, H. Wang, Q. Wang, S. Chu and Y. Cui, *ACS Nano*, 2020, **14**(5), 6348–6356.
4 M. C. Turner, Z. J. Andersen, A. Baccarelli, W. R. Diver, S. M. Gapstur, *et al.*, *Ca-Cancer J. Clin.*, 2020, **70**(6), 460–479.
5 S. Chowdhury, S. Dey and K. R. Smith, *Nat. Commun.*, 2018, **9**(1), 318.
6 H. Liu, S. C. Zhang, L. F. Liu, J. Y. Yu and B. Ding, *Adv. Funct. Mater.*, 2020, **30**, 1909554.
7 R. S. Barhate and S. Ramakrishna, *J. Membr. Sci.*, 2007, **296**(1), 1–8.
8 C. S. Wang and Y. Otani, *Ind. Eng. Chem. Res.*, 2013, **52**(1), 5–17.
9 A. Ghosal, S. Sinha-Ray and A. L. Yarin, *Polymer*, 2016, **85**, 19–27.
10 Y. Xu, X. Zhang, D. Teng, T. Zhao, Y. Li and Y. Zeng, *Nano Res.*, 2022, **15**(8), 7549–7558.
11 L. Wang, Y. Gao, J. Xiong, W. Shao, C. Cui, N. Sun, Y. Zhang, S. Chang, *et al.*, *J. Colloid Interface Sci.*, 2022, **606**, 961–970.
12 L. Huang, S. Xu, Z. Wang, K. Xue, J. Su, *et al.*, *ACS Nano*, 2020, **14**(9), 12045–12053.
13 J. Xue, T. Wu, Y. Dai and Y. Xia, *Chem. Rev.*, 2019, **119**(8), 5298–5415.
14 Y. Deng, T. Lu, X. Zhang, Z. Zeng, R. Tao, Q. Qu, *et al.*, *J. Membr. Sci.*, 2022, **660**, 120857.
15 Y. Deng, T. Lu, J. Cui, W. Ma, Q. Qu, X. Zhang, Y. Zhang, *et al.*, *Sep. Purif. Technol.*, 2022, **294**, 121093.
16 H. Liu, S. Zhang, L. Liu, J. Yu and B. Ding, *J. Mater. Chem. A*, 2020, **8**(36), 18955–18962.
17 Y. Li, L. Cao, X. Yin, Y. Si, J. Yu and B. Ding, *J. Colloid Interface Sci.*, 2020, **578**, 565–573.
18 X. Chen, Y. Xu, M. Liang, Q. Ke, Y. Fang, H. Xu, X. Jin and C. Huang, *J. Hazard. Mater.*, 2018, **347**, 325–333.
19 X. Zhao, Y. Li, T. Hua, P. Jiang, X. Yin, J. Yu and B. Ding, *Small*, 2017, **13**(11), 1603306.
20 H. Liu, S. Zhang, L. Liu, J. Yu and B. Ding, *Adv. Funct. Mater.*, 2019, **29**(39), 1904108.
21 T. T. Li, X. Cen, H. T. Ren, F. Sun, Q. Lin, C. W. Lou and J. H. Lin, *Polymers*, 2019, **11**, 1307.
22 M. Zhu, J. Han, F. Wang, W. Shao, R. Xiong, Q. Zhang, H. Pan, *et al.*, *Macromol. Mater. Eng.*, 2017, **302**(1), 1600353.
23 W. Ma, H. Qi, Y. Zhang, M. Lin, Y. Qiu and C. Zhang, *Polymers*, 2023, **15**(6), 1459.
24 H. Zhang, Q. Zhen, Y. Liu, R. Liu and Y. Zhang, *Results Phys.*, 2019, **12**, 1421–1428.
25 Y. Zhu, X. Gu, Z. Dong, B. Wang, X. Jin, Y. Chen, *et al.*, *RSC Adv.*, 2023, **13**(12), 7857–7866.
26 G. Zheng, Z. Shao, J. Chen, J. Jiang, P. Zhu, *et al.*, *Nanomaterials*, 2021, **11**(10), 2567.
27 H. Li, H. Huang, X. Meng and Y. Zeng, *J. Polym. Sci., Part B: Polym. Phys.*, 2018, **56**(13), 970–977.
28 X. Lin, M. Lin, T. Li, H. Lu, H. Qi, *et al.*, *Polymers*, 2023, **15**, 3365.
29 C. H. Lee, K. C. Hung, M. J. Hsieh, S. H. Chang, J. H. Juang, *et al.*, *Nanomed. Nanotechnol. Biol. Med.*, 2020, **24**, 102123.
30 S. Zhang, M. Zhang, R. Bai, L. Kong, H. Yang, *et al.*, *Mater. Today Chem.*, 2022, **26**, 101246.
31 L. Zheng, M. Zhu, B. Wu, Z. Li, S. Sun and P. Wu, *Sci. Adv.*, 2021, **7**(22), eabg4041.
32 C. Wang, Y. Liao, H. Y. Yu, Y. Dong and J. Yao, *Carbohydr. Polym.*, 2023, **319**, 121175.
33 T. Lu, J. Cui, Q. Qu, Y. Wang, J. Zhang, R. Xiong, W. Ma and C. Huang, *ACS Appl. Mater. Interfaces*, 2021, **13**(20), 23293–23313.
34 H. Liu, C. Cao, J. Huang, Z. Chen, G. Chen and Y. Lai, *Nanoscale*, 2020, **12**(2), 437–453.
35 T. T. Li, Y. Fan, X. Cen, Y. Wang, B. C. Shiu, H. T. Ren, *et al.*, *Nanomaterials*, 2020, **10**(10), 2025.
36 M. Tang, S. C. Chen, D. Q. Chang, X. Xie, *et al.*, *Sep. Purif. Technol.*, 2018, **198**, 137–145.
37 R. Thakur, D. Das and A. Das, *Sep. Purif. Rev.*, 2013, **42**(2), 87–129.

38 S. Wang, X. Zhao, X. Yin, J. Yu and B. Ding, *ACS Appl. Mater. Interfaces*, 2016, **8**(36), 23985–23994.
39 X. Gao, Z. K. Li, J. Xue, Y. Qian, L. Z. Zhang, J. Caro and H. Wang, *J. Membr. Sci.*, 2019, **586**, 162–169.
40 Z. Yi, P. Cheng, J. Chen, K. Liu, Q. Liu, M. Li, *et al.*, *Ind. Eng. Chem. Res.*, 2018, **57**(28), 9269–9280.
41 Y. Yang, S. Zhang, X. Zhao, J. Yu and B. Ding, *Sep. Purif. Technol.*, 2015, **152**, 14–22.
42 X. Li, N. Wang, G. Fan, J. Yu, J. Gao, G. Sun and B. Ding, *J. Colloid Interface Sci.*, 2015, **439**, 12–20.
43 S. Zhang, H. Liu, N. Tang, S. Zhou, J. Yu and B. Ding, *Adv. Mater.*, 2020, **32**(29), 2002361.
44 K. S. Han, S. Lee, M. Kim, P. Park, M. H. Lee and J. Nah, *Adv. Funct. Mater.*, 2019, **29**(37), 1903633.
45 B. Cao, F. Qian, M. Ye, Y. Guo, S. Wang, J. Lu and Y. Han, *Build. Environ.*, 2021, **202**, 108015.
46 J. Li, P. Wang, D. Wu and D. R. Chen, *Sep. Purif. Technol.*, 2020, **234**, 116086.
47 S. Park, Y. H. Joe, J. Shim, H. Park and W. G. Shin, *J. Hazard. Mater.*, 2019, **365**, 440–447.
48 M. Lin, J. Shen, B. Wang, Y. Chen, C. Zhang and H. Qi, *RSC Adv.*, 2023, **13**(44), 30680–30689.